ORNL/TM-2023/2984

Development of Optical Fiber–Based Sensors for Nuclear Microreactor Structural Health Monitoring

Anthony Birri
Daniel C. Sweeney
Holden C. Hyer
Brandon Schreiber
Christian M. Petrie

OAK RIDGE National Laboratory

ORNL IS MANAGED BY UT-BATTELLE LLC FOR THE US DEPARTMENT OF ENERGY

ORNL/TM-2023/2984

Nuclear Energy and Fuel Cycle Division

Development of Optical Fiber–Based Sensors for Nuclear Microreactor Structural Health Monitoring

Anthony Birri,
Daniel C. Sweeney,
Holden C. Hyer,
Brandon Schreiber,
Christian M. Petrie

Milestone M3AT-23OR0804071
August 2023

Prepared by
OAK RIDGE NATIONAL LABORATORY
Oak Ridge, TN 37831
managed by
UT-Battelle LLC
for the
US DEPARTMENT OF ENERGY
under contract DE-AC05-00OR22725

CONTENTS

LIST OF FIGURES

ACKNOWLEDGMENTS

This work is supported by the Microreactor Program of the US Department of Energys Office of Nuclear Energy. The authors acknowledge Bob Sitterson for his assistance in bonding the optical fiber-based sensors developed herein to test specimens.

ABBREVIATIONS

FBG	fiber Bragg grating
FFT	fast Fourier transform
FPC	Fabry–Pérot cavities
FRM	Faraday rotating mirror
FSR	free spectral range
FUT	fiber under test
LCI	low-coherence interferometry
LDV	laser Doppler vibrometry
MR	Nuclear Microreactor
MRP	Microreactor Program
MZI	Mach–Zehnder interferometer
OFDR	optical frequency domain reflecometry
ORNL	Oak Ridge National Laboratory
PWR	pressurized water reactor
SHM	structural health monitoring
SMR	small modular reactor
SNR	signal-to-noise ratio
TLS	tunable laser source

SUMMARY

This report provides an experimental assessment of two different optical fiber–based acoustic sensors that are being investigated for application in nuclear microreactors to enhance structural health monitoring capabilities. Optical fibers are resilient in high-temperature and high-radiation environments, have a small sensor footprint, are immune to electromagnetic interference, and are capable of spatially distributed sensing. The two sensors investigated here are (1) Fabry–Pérot Cavities (FPCs) between two copper-coated fibers, embedded in nickel capillary tubes and (2) type-I fiber Bragg grating (FBG) arrays contained within metal capillary tubes. These sensors can be interrogated using low-coherence interferometry or swept wavelength interferometry, respectively, to measure the resonant frequencies of the components or systems to which these sensors are bonded. The FPC developed herein has been subjected to temperatures up to nearly 800°C while tack-welded to a tubular test specimen. Even at the highest temperatures, the measured resonant frequencies compared well with those obtained using an accelerometer that was bonded to an unheated portion of the specimen. The FBG array was tested in multiple bonding configurations to a tubular test specimen, all at room temperature, with the understanding that high temperature (i.e., type II) FBGs could be used to obtain similar data at high temperatures; the FBG array data were validated with noncontact laser vibrometry, which is being used at Los Alamos National Laboratory to relate acoustic signatures to component stresses and/or structural defects. The goal of this work is to identify the most promising techniques that are also compatible with operation in a microreactor environment.

Experimental results from the FPC indicated that the sensor provided validated frequency content (in terms of the observable resonant frequencies) up to the furnace set point of 800°C. The frequency spectra obtained during the furnace heating and cooling cycle indicated some level of nonrecoverable FPC displacement, and also that the FPC lost signal at some point during furnace cooling. In general, the FPC experimental results are promising given the survivability up to 800°C. The failure was likely the result of oxidation of the copper coating on the fiber at high temperatures, rendering it brittle and more susceptible to fracture caused by differential thermal contraction during cooling. This failure mode could be mitigated using a more inert coating material (such as gold) or by controlling the atmosphere surrounding the fiber. Experimental results from the FBG array indicate that the sensor also provided validated frequency content, regardless of the bonding technique. Results also indicated that the signal-to-noise ratio and the ability to recover the mode shapes depends on the bonding technique used to join the FBG array to the sample.

1 INTRODUCTION

Nuclear microreactors (MRs) have the potential to tap into nontraditional energy markets and provide electricity for several years in unique implementations that may have otherwise relied on CO_2-emitting energy production processes. MRs are distinct from small modular reactors (SMRs) and conventional, large-scale power reactors such as pressurized water reactors (PWRs) or boiling water reactors (BWRs) in that they have significantly lower energy outputs, generally less than 20 MW. These lower energy outputs allow MRs to be significantly smaller than other reactor classes: MRs are small enough to be portable, enabling implementation in remote or rural communities, industrial implementations in which large diesel generators would have otherwise been needed, military installations, and natural disaster recovery use cases [1, 2]. Other promising characteristics of the MR class are the ability to operate for several years without refueling [3], inherently safe design features such as passive safety systems and melt-tolerant fuels [4], and autonomous reactor operation controls. Several private entities are currently developing MR designs for future deployement, including Westinghouse [5], Oklo [6], X-Energy [7], NuScale [4], LeadCold [8], Ultra Safe Nuclear Corporation [4], and more [4].

In general, these MR designs involve high-temperature gas or liquid sodium cooling with heat pipes; as such, the Microreactor Program (MRP) within the US Department of Energy's Office of Nuclear Energy is conducting research in support of these MR subclasses [7, 9, 10, 11]. The MRP is developing two nonnuclear systems to serve as experimental test beds to evaluate the thermal–hydraulic and thermomechanical behavior of MR components [12, 13]. The MRP is also developing a nuclear test platform with the intent to allow end users to improve integration of autonomous control algorithms for a variety of reactor operations [14]. The program has identified several technical areas that require additional technology maturation to enable MR designs, such as high-temperature moderator materials, heat transfer and power conversion, instrumentation and sensors, legacy fuel data, and advanced structural material manufacturing and testing [15].

Automated or autonomous control of MRs will rely on recent advances in instrumentation to provide a wealth of data regarding the current status and health of the reactor. In particular, improved structural health monitoring (SHM) would provide invaluable data to inform operators of potential signs of future maintenance needs that could be addressed during future planned outages, thereby preventing costly unplanned reactor shut downs. If SHM data could be acquired in situ during reactor operation, they could help mitigate the need for time-consuming manual examinations and thus reduce operation and maintenance costs. Some MR concepts will expose core materials to harsher conditions than those of conventional light-water reactors [16]. These MRs' small size and extremely high operational temperatures (exceeding 800°C in some cases[10, 17]) will likely result in large differential thermal strain gradients and large variations in radiation-induced dimensional changes. For these reasons, the ability to monitor the structural health of in-core MR components is particularly attractive. Acoustic measurements and other vibration-based methods have been used extensively in civil infrastructure, where a network of sensors can capture the vibrational content of a system or structure. Changes in the resonant frequencies or frequency modes can be used to infer the size, location, and severity of structural damage [18, 19]. In fact, vibration-based SHM has been applied to nuclear reactors in several cases [20, 21, 22, 23].

Enabling SHM in MRs, particularly for diagnostics of the structural health of in-core components, will require the sensors that capture the vibrational content to be particularly robust to extremely high neutron–gamma doses and extreme temperatures. As mentioned previously, the sensors might be subjected to temperatures exceeding 800°C. Depending on the design lifetime of in-core components and their

proximity to the center of the core, the sensors could be subject to fast neutron fluences on the order of 10^{21}–10^{22} n/cm^2, as estimated based on flux calculations from neutronics models of a heat pipe–cooled microreactor [24]. Additional survivability considerations for MRs are discussed in a previous report [16].

Optical fiber–based sensors are promising for acoustic sensing in MRs for SHM. In general, intrinsic sensors such as fiber Bragg gratings (FBGs) and Fabry-Pérot Cavities (FPCs) have shown survivability up to and exceeding 1,000°C [25, 26]; both of these intrinsic sensors can measure vibrational frequencies by rapid acquisition of their reflected spectral shifts using spectrometric or interferometric techniques [27, 28, 29, 30, 31]. Static spectral shifts have been resolved in unmodified optical fibers by using optical frequency domain reflectometry (OFDR) with adaptive reference techniques at temperatures up to 1,000°C [32], suggesting that the fibers and interrogation techniques could also be used to measure acoustic vibrations at these same temperatures. Although the hardware used previously to measure static spectral shifts at high temperatures is limited to lower frequencies, other previous works have demonstrated that OFDR measurements can be performed at frequencies greater than 1 kHz [33, 34].

Optical fiber–based sensors also have shown good survivability in extreme radiation fields. Minimal signal attenuation has been observed in bulk amorphous fused silica and in pure silica core optical fibers up to a fast neutron fluence of 2.4×10^{21} n/cm^2 and about 10^{21} n/cm^2, respectively [35, 36]. Furthermore, the ability to resolve spectral shift has also been demonstrated up to a fast neutron fluence of about 10^{21} n/cm^2 [36]. Optical fiber–based sensors experience significant blue wavelength shifts in their reflected spectra owing to fast neutron exposure and the resulting compaction of the silica glass network [35, 36, 37, 38, 39]. However, this phenomenon is less of a concern for vibration measurements because these wavelength shifts would only represent a low-frequency offset that would not prevent vibration measurements.

In general, other vibration sensors such as piezoelectric sensors and strain gauges have not been demonstrated to survive either up to similar temperatures or up to similar fast neutron fluences. Some intrinsic FBGs may degrade significantly under extreme neutron fluence [36, 40], but their high-temperature survivability still makes them attractive candidates for many MR applications, partiuclarly those further from the center of the core where the neutron fluence is lower. FPCs are anticipated to be more robust to extreme radiation levels because their sensing mechanism only relies on maintenance of a gap between two fiber end faces. Additional details on how FPCs function are provided in Section 2.1). Furthermore, a precedent exists for using FPCs in an extreme radiation environment because the Spallation Neutron Source at the US Department of Energy's Oak Ridge National Laboratory (ORNL) currently deploys more than 20 FPC-based vibration sensors [41].

Given the demonstrable applicability of optical fiber–based sensors in extreme environments, ORNL is investigating optical fiber–based sensors for acoustic monitoring in MRs. Specifically, FPCs and FBGs are both being investigated for applicability in MR environments. The overall goal is to assess the high-temperature survivability of sensors that are designed, packaged, and bonded to relevant MR components and are capable of surviving the environmental conditions that are expected for MR applications. This report describes recent high-temperature testing of various optical fiber–based acoustic sensing, including recommendations for sensors and bonding techniques that are most appropriate for MR applications.

2 OPTICAL VIBRATION SENSORS AND INTERROGATION EQUIPMENT

2.1 Fabry–Pérot Cavities

The FPCs used in this work comprised two copper-coated optical fibers that were inserted into a nickel capillary tube, with a small gap between both end faces. The ends of both fibers were cleaved to ensure a flat face. Copper-coated fibers were chosen over more conventional polymeric coatings because most polymers start to decompose at less than 250°C—well below the temperatures expected for MR applications. The copper coating was bonded to the nickel capillary using laser welding along regions located about 5 mm from the end faces of each fiber by using a Renishaw AM400 laser powder bed fusion system. Additional details on the specifications and fabrication processes of these sensors are detailed in a previous report [16]. The FPC design considered herein is illustrated in Figure 1. FPCs are effectively point sensors that can be interrogated to measure dynamic changes in the length between the two fiber end faces.

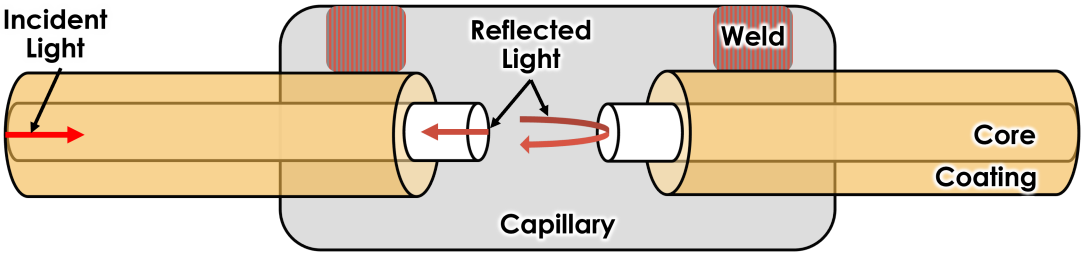

Figure 1. Example FPC fabricated by inserting cleaved copper-coated fibers into a short section of a nickel capillary tube.

Under the assumption that a broad enough spectrum of light is injected into the FPC, the reflected spectrum contains a series of peaks corresponding to constructive and destructive interference of light waves reflecting from the surface of both fiber end faces. The interference pattern arises based on certain wavelengths being more or less in phase based on the gap size. The interrogation systems considered herein enable resolution of several peaks in these interference patterns for the relevant gap sizes (30–270 μm). The free spectral range (FSR) is defined as the spacing (in nanometers) between two successive peak maxima, and FSR and cavity length are approximately inversely related; therefore, the FSR is expected to decrease as the FPCs are heated due to thermal expansion of the capillary tube. Because glass end faces are used as the reflective surfaces for the FPCs in this study, the FPCs are particularly low-finesse designs (i.e., the peaks in the interference patterns have large full width at half maximum relative to the FSR), whereas an FPC with a metal end face would otherwise have much smaller full width at half maxiumum for the same FSR.

2.2 Fiber Bragg Gratings

FBGs are fundamentally different from FPCs in that they are inscribed into the core of a length of optical fiber and do not involve cleaved fiber end faces. FBGs are laser inscribed modulations of the refractive index along the axial length of the fiber. An FBG array can be fabricated by inscribing multiple FBGs along the length of a single fiber, enabling quasi-distributed sensing. A cascade of FPCs has been demonstrated in multiple cases with a range of fabrication techniques and specifications [42, 43, 44, 45], but such quasi-distributed sensors remain solely considered within the research domain and are not

commercially available. A depiction of an FBG is shown in Figure 2; several modulations (typically thousands) of refractive index exist per FBG, but a single FBG acts as a point sensor. Multiple FBGs, separated by lengths of unmodified fiber, enable quasi-distributed sensing.

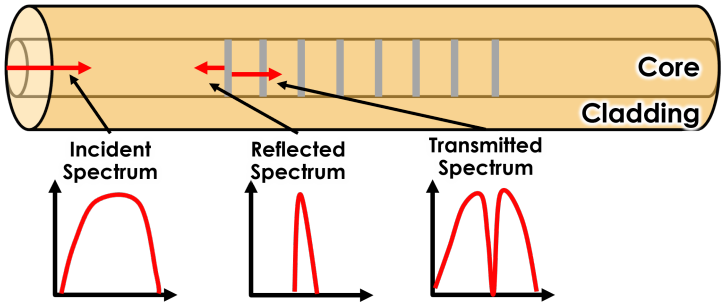

Figure 2. Depiction of an FBG.

The FBGs used herein were draw tower gratings written in low-bend-loss fiber (LBL-1500-125) from FBGS Technologies GmbH. The FBG array consisted of 29 FBGs that were each 10 mm long and separated from one another by 2 cm. The FBG reflectivities ranged from 20% to 30%. The FBGs' center wavelengths were 1,470–1,610 nm; each consecutive FBG was separated in peak wavelength by 5 nm. These FBGs were not high-temperature FBGs, and the manufacturer lists an operational temperature limit of 200°C (possibly just the coating's temperature limit). Regardless, arrays of femtosecond laser-inscribed FBGs are available commercially from multiple vendors and have been demonstrated to survive conditions exceeding 1,000°C. Therefore, the FBG array used herein allows researchers to determine the feasibility of such an array for point or quasi-distributed vibration sensing at room temperature, with the understanding that high-temperature FBG arrays are available. The vibrations are sensed via rapid acquisition of the reflected spectra of the FBG array when the FBG array is mechanically coupled to a vibrating specimen. The time-dependent shift in the peak frequencies for each of the respective FBGs can be used to identify the vibrational content at each of the FBG locations. The reflected spectrum (for one instance in time) is shown in Figure 3, along with a depiction of the FBG array, aligned spatially with the respective peaks in the spectrum. In this depiction, the FBG inscribed fiber is within a capillary tube bonded to a test specimen.

2.3 Swept-Wavelength Interferometry

FBGs and FPCs can be interrogated using swept-wavelength interferometry using commercially available instruments, such as the Hyperion si55 (Luna Innovations, Inc., Blacksburg, Virginia, USA). This instrument employs a tunable laser source (TLS) to quickly sweep over its 160 nm wavelength range and couple that light into a fiber under test (FUT). The intensity of the light reflected by features in the FUT (e.g., FBGs, FPC) is coupled back into the optical network and recorded by a photodetector. Features, such as the FPC lengths or the Bragg wavelengths of FBGs, can be isolated from this intensity profile and used as measurands [46]. For FPCs specifically, the peak locations in the interference pattern can be used to calculate an absolute cavity length. Recently, methods were developed to measure change in cavity length with nanometer precision measurements by utilizing multiple peaks acquired during a single measurement frame, in a hybrid method involving rough FSR calculations in combination with precise phase tracking [47]. Furthermore, these features can be identified and isolated via a combination of hardware and software on an instrument to decrease the quantity of data transferred to the end user and ultimately increase the sampling rate of the system. For example, the Hyperion si155 can acquire data from four channels

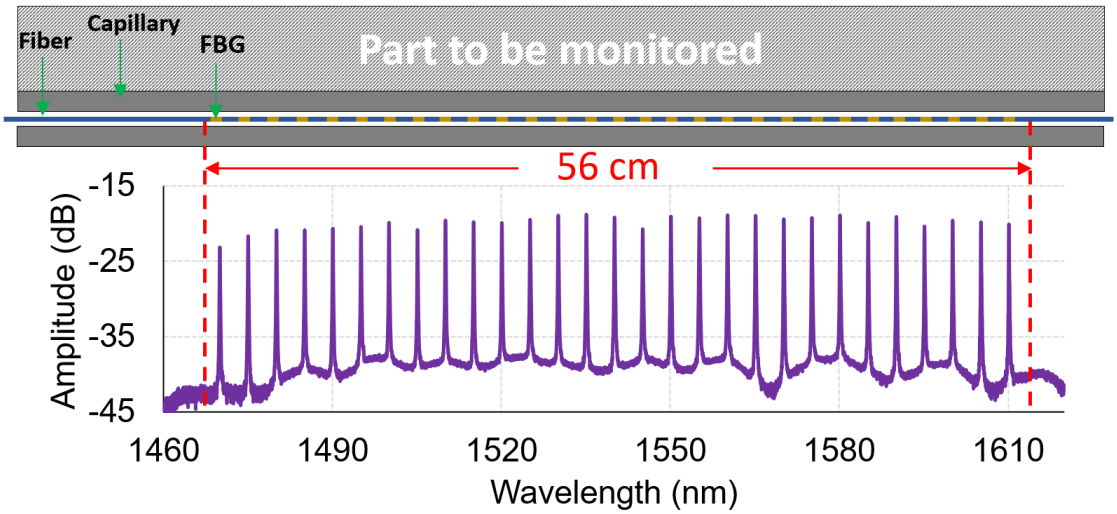

Figure 3. Depiction of the FBG array and the corresponding reflected spectrum.

simultaneously at a rate of 1 kHz per channel.

2.4 Low-Coherence Interferometry System

In addition to swept-wavelength interferometry, low-coherence interferometry (LCI) can also be used to interrogate FPCs. LCI instruments employ a combination of two interferometers to mitigate polarization artifacts: an FPC located remotely at the intended sensor location and a local Michelson interferometer that is positioned in a controlled environment near the data acquisition system [48, 49]. The FPC is interrogated using light from a superluminescent diode before coupling into the Michelson interferometer. The two arms of the Michelson interferometer are offset, ideally at a phase angle of $\pi/2$ (quadrature), and light entering the Michelson interferometer from the FPC is coupled equally into each arm. Each Michelson interferometer arm terminates with a Faraday rotating mirror (FRM), which reflects light back into a coupler where it interferes before being recorded by two photodetectors recording the interference pattern in a pont-by-point fashion. A third photodetector can be added to compensate for changes in intensity [50]. Because the photodetectors record the intensity of a specific point in the interference pattern, rather than relying on an intensity spectrum as in swept-wavelength interferometry, the LCI system's measurements can be much faster. In the present work, measurements were recorded at a rate of 100 kHz with nanometer-scale precision [49]; in principle, these measurements could be recorded much faster.

Although significantly faster than swept-wavelength interferometry with similar precision, LCI measurements have three notable limitations: (1) the measurement range limit imposed by the coherence length of the superluminescent diode, (2) the relative nature of the LCI measurements, and (3) the fact that the LCI system provides data only at a single measurement location. The coherence length of the superluminescent diode limits the measurable changes in FPC length to ±20 μm of the initial reference measurement. This limit is significantly smaller than the range of FPC lengths measurable using swept-wavelength interferometry, which can measure deflections about fivefold larger (0.1–1 mm). The relative nature of LCI measurements arises from the point-by-point nature of the measurement and inability to calculate absolute FPC length on the fly without a priori knowledge. However, when the changes in FPC

length are small and occur quickly (such as vibration measurements) , the LCI system is an extremely effective instrument.

3 VALIDATING VIBRATION SENSORS

3.1 Piezoelectric Accelerometer

Accelerometers measure acceleration and can be fabricated via several different processes. Most accelerometers are designed for relatively low-temperature operation. Commercially available accelerometers are typically designed to produce a voltage change ΔV proportional to an acceleration a, specified by the following relation:

$$\Delta V = S_p a, \tag{1}$$

where the calibrated sensitivity $S_p = 48.23$ mV/g at 80 Hz is given in the accelerometer data sheet, which also states the usable frequency range of 20 Hz to 10 kHz. The 8201-0025-125 uniaxial accelerometer (TE Connectivity, Shenzhen, China) used in this work exhibited <8% transverse sensitivity and was oriented parallel to the long axis of the test article during testing. The accelerometer voltage ΔV was monitored by a LabJack T7 data acquisition system (LabJack Corporation, Lakewood, Colorado, USA) using a 16 bit analog-to-digital converter at a rate of 20 kHz (±10 V range). Assuming a constant mass, the acceleration a is proportional to the force applied to the accelerometer. For vibration measurements, the strain applied to the accelerometer is measured directly by monitoring ΔV, and subsequent spectral analysis is used to determine the system response.

Accelerometers provide a reference measurement for comparing all optical fiber-based acoustic measurements. However, the present accelerometer is not suitable for use in MRP-relevant conditions because of its relatively low functional temperature range (−40°C to 125°C). Several more exotic piezoelectric transducers have been shown to be resistant to well over 1 MGy at MRP temperatures of 500°C–800°C [51]. However, even with more exotic materials, piezoelectric accelerometers provide only single-point measurements. They require relatively lengthy cable runs to transmit power and data, which could distort the output signal. Moreover, extensive literature review indicates that their neutron radiation tolerance for in-core applications has not been demonstrated.

3.2 Laser Vibrometer

Laser Doppler vibrometry (LDV) leverages the concepts of Doppler shift and interferometry. A laser is directed onto the surface of a vibrating object, and the reflected light is coupled with a reference beam created by splitting an incident laser beam into the measurement beam and the reference beam [52]. This combined light is then directed into a photodetector.

When the measurement beam is reflected by a vibrating object, the measured frequency shift (f_D) of the wave is calculated as follows:

$$f_D = \frac{2V}{\gamma}, \tag{2}$$

where V is the monitored objects velocity, and γ is the wavelength of the emitted wave (633 nm for the helium–neon laser used in this LDV system). To calculate the object's velocity, the Doppler frequency shift s is determined via interferometry: the superimposed reference beam and measurement beam reveal the frequency shift. The optical path length of the reference beam remains unchanged throughout the measurement. However, the measurement beams optical path length varies as the reflecting surface of the

target object vibrates, resulting in a detectable change in frequency and phase of the reflected light. When the reflected measurement beam is coupled with the reference beam, the interfering light waves create an interference pattern signal that reveals the Doppler shift in frequency. Figure 4 illustrates the basic components and layout of this system.

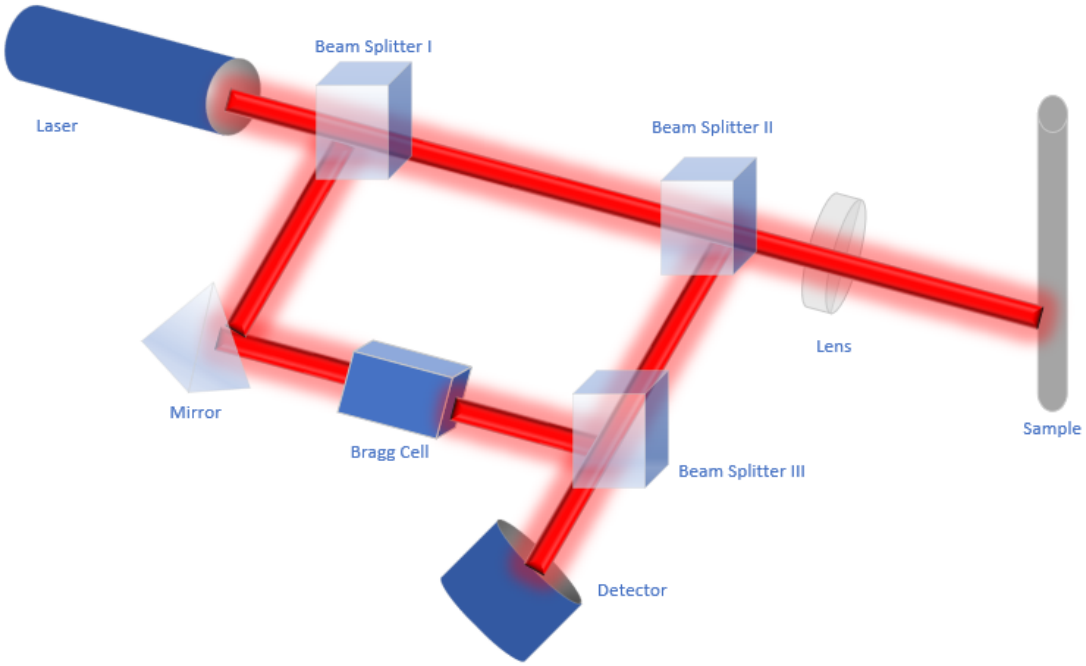

Figure 4. Laser Doppler vibrometer topology.

LDV provides many advantages over traditional methods of vibration measurement, including conventional accelerometers. LDV is a noncontact method, so it does not damp the vibrations on the measured object, whereas affixing an accelerometer not only changes the system's total mass but also can change the structure's local stiffness. These factors introduce damping into the system, thereby shifting the measured frequency [52]. LDV measurements also allow for remote measurement of objects that are difficult to physically access and objects to which contact sensors cannot easily be affixed. In systems that may be wet, hot, or slick, affixing a contact measurement device may not be practical.

However, LDV systems have some drawbacks, especially cost and size. Because LDV measures only a single point, gathering data about vibration along the length of an object requires multiple beams or a mechanical method of repositioning the beam. The physical space required by an LDV system by both the housing for the beam emitter and the standoff distance required for proper signal-to-noise ratio (SNR) presents a challenge for many in situ applications. Another drawback of LDV is the SNR heavily depends on the reflectivity of the measured object. In some applications, affixing a retroreflective material to the objects surface can circumvent this drawback and ensure a strong signal. The need for adhering a separate material renders this solution impractical for some applications. Finally, safety regulations surrounding the use of lasers may make LDV systems unsuitable for all applications. MR applications are unlikely to allow optical access for LDV systems to perform in situ vibration sensing. Therefore, although LDV is useful for technique development and validating measurements by other sensors, its application for MRs would be limited to ex-core components (minimal radiation dose) that allow optical access to the component of

interest.

The LDV system used in the FBG verification experiment discussed in Sections 4.1 and 5.1 was a combination of the VibroFlex Neo and the VibroFlex Connect Front-End (Polytec, Plymouth, Michigan, USA). The measurement beam was produced by the VibroFlex Neo and was then demodulated and analyzed by the Connect Front-End. This setup is detailed in Figure 5.

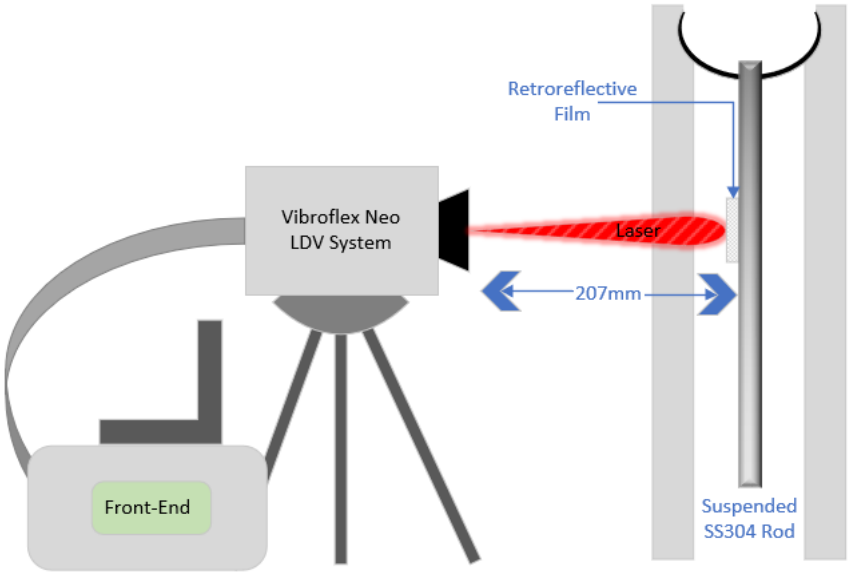

Figure 5. Laser Doppler vibrometer experimental setup.

This LDV system can measure a wide range of velocities and displacements. Velocity readings can be taken between as low as 1 mm/s up to 12 m/s. The displacement range is even broader, covering 10 nm up to 200 mm. Velocity windows of ±100 mm/s and displacement windows of ±20 mm were used to capture the vibrational data from the measured rod in this experiment. These data can be measured at a rate up to 50 kHz, although 20 kHz was used for this experiment to improve the SNR.

4 EXPERIMENTAL METHODS

4.1 Low-Temperature Fiber Bragg Grating Test

To test various coupling methods of the FBG fiber and compare them with a noncontact method of measurement for verification purposes, an experiment used the LDV described in Section 3.2 in conjunction with the FBGs to simultaneously measure and record vibration data from a solid 304 stainless-steel rod with a diameter of 0.635 cm.

This LDV uses a helium–neon laser with a wavelength of 633 nm and a cavity length of 204 ± 1 mm. The cavity length combined with the 3 mm setback of the lens from the metal housing yields a recurring visibility maxima every 204 mm beginning at 207 mm. This standoff distance was used to obtain the results discussed in Section 5.1.

Once the data were captured using the combination of front-end and laser, they were analyzed using the VibSoft software package (Polytec). This software uses the fast Fourier transform (FFT) procedure to

generate a measured frequency spectrum. VibSoft allows further manipulation of the obtained data, such as narrowing the window of measured frequencies. To focus on only the first three expected vibrational modes of the rod and to omit the low-frequency pendulum motion of the rod after excitation, a window range of 50 to 500 Hz was used.

While measuring vibration data were measured via the LDV system, the Hyperion system discussed in Section 2.3 was used to collect data from an FBG fiber coupled to the rod. This experiment verified the accuracy of the contact FBG readings by a precise noncontact method. The FBG array has the added benefit of being able to acquire the multiple measurement points along the length of the array to reconstruct the vibrational modes.

Four methods of coupling the FBG fiber to the rod were used in this experiment and are detailed in Figure 6. (1) The top and bottom ends of the fiber were taped directly to the rod. (2) The fiber was taped directly to the rod along its length. (3) The fiber was fed through a 0.25 mm (0.010 in.) diameter capillary, and then the capillary was tack-welded to the rod with small stainless-steel strips. (4) The fiber was fed through the tack-welded capillary, and then the capillary was taped along its length to maximize acoustic coupling. For each of these coupling methods, the fiber position was the same, and the last FBG coincided with the bottom end of the rod.

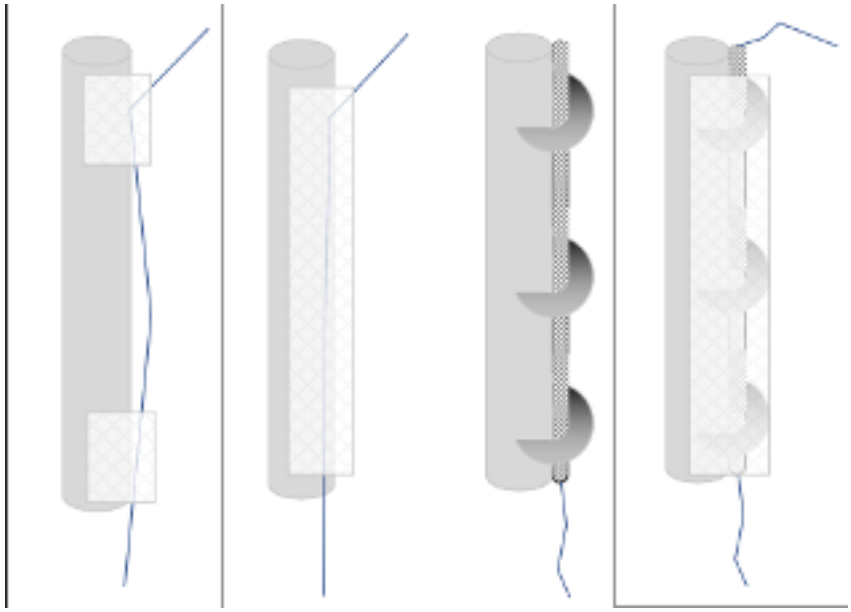

Figure 6. Methods for coupling FBG fibers to the rod for acoustic testing. (left to right) Bare fiber taped at top/bottom, bare fiber taped along length, fiber fed through tack-welded capillary, fiber fed through tack-welded capillary and taped along length.

Although tapes and many adhesives are unsuitable for high-temperature applications, Petrie et al. [53] showed that fiber sensors can be embedded directly into metal components. The present experiment was conducted at low temperatures, so approximating embedding with tight coupling along the length was deemed sufficient to replicate many of these advantages without the complication of actually embedding the fiber into the rod.

4.2 High-Temperature Fabry-Pérot Cavity Test

An experiment was conducted to test the survivability of an FPC sensor up to a furnace set-point temperature of 800°C. The experimental setup was arranged as shown in Figure 7. The FPC was tack-welded to a 304 stainless-steel tubular specimen with an inner diameter of 1.73 cm and an outer diameter of 1.91 cm. The FPC was tack-welded to the outside of the specimen using small strips of stainless steel. The top of the test specimen passed out of the top of the furnace and was supported by a high-temperature string. Thus, the specimen was considered in the free–free configuration, as per Euler–Bernoulli beam theory, in that it was not pinned down or bonded to any other object or surface. The physical contact with the wire holding the specimen makes this configuration an approximation with respect to the specimen's expected vibrational behavior. The piezoelectric accelerometer was bonded to the specimen in the non-heated region using high-temperature tape. An extension fiber connected the FPC to the LCI system, and an extension wire connected the accelerometer to the LabJack T7. The extension fiber was also periodically connected to the Hyperion si155 for spectral measurements to measure the absolute FPC length. The furnace was an Evenheat Model SB 718 SAP. Not shown in the image is a type-K thermocouple, which was fixed adjacent to the FPC. Thermocouple data were logged using a Grant Squirrel SQ2020 Data Logger.

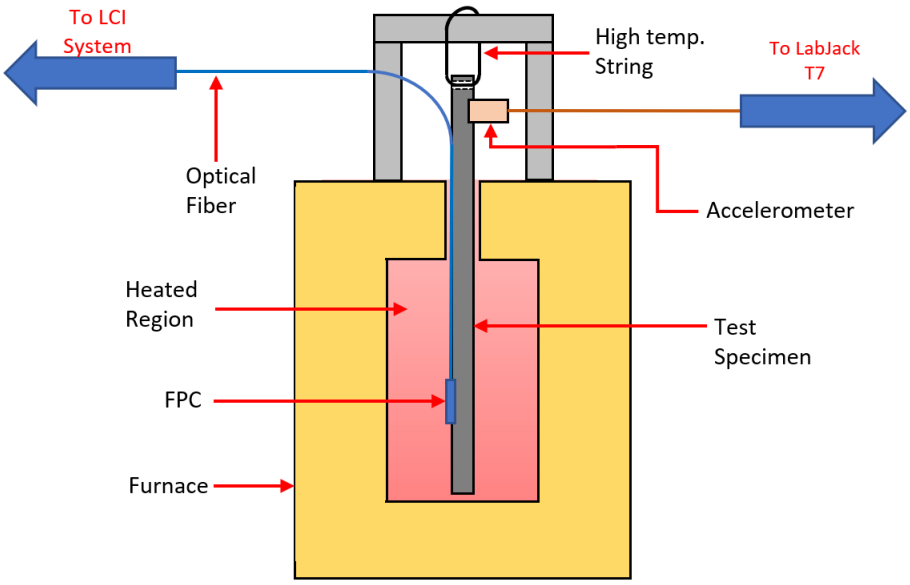

Figure 7. Schematic of the high-temperature experiment. An FPC sensor was bonded to a tubular specimen and a piezoelectric vibration sensor was attached in the unheated region.

The heating profile to which the FPC was subjected is shown in Figure 8. Generally, the temperature was increased from room temperature (23°C) to a furnace set point of 800°C; the furance setpoint temperature was increased to 100°C and then to 200°C; all later increases were in increments of 50°C. The entire heating cycle was completed in approximately 6 h. The vertical lines in Figure 8 indicate times at which either a scan was taken with the Hyperion si155 to capture the reflected spectra from the FPC, or a vibrational test was conducted to acquire frequency content from both the FPC and the accelerometer. Each of these tests consisted of striking the test specimen 10–15 times with a solid metal rod to cause the

specimen to vibrate at its natural resonant frequencies. A 2–4 s pause was held between strikes. The time-dependent FPC displacement data were recorded at an acquisition rate of 100 kHz, and the accelerometer voltage data were recorded at an acquisition rate of 20 kHz. Two types of tests were conducted: (1) the accelerometer was bonded to the specimen to verify the FPC data, and (2) the accelerometer was not bonded, enabling data collection while the specimen was not significantly damped by the accelerometer, which is relatively bulky.

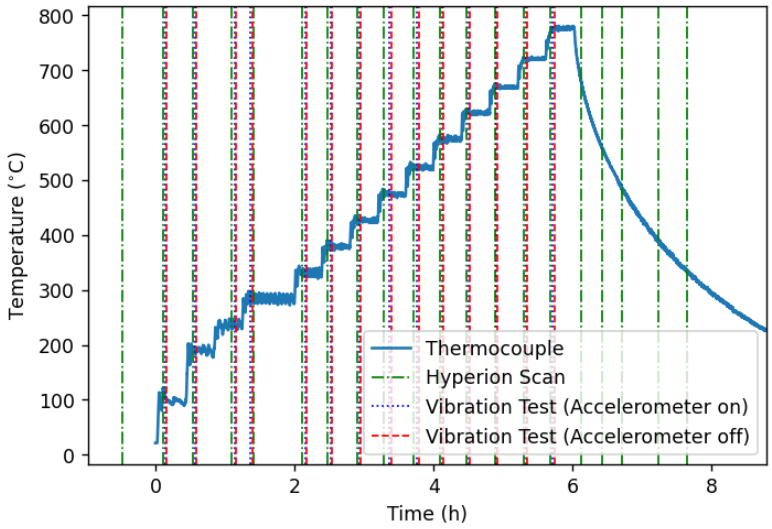

Figure 8. Time-dependent heating profile to which the FPC sensor was subjected. Vertical lines indicate times at which certain data were acquired.

The specimen strikes were detected by identifying large jumps in the moving average of the variance of the FPC deflection data. The strike times associated with these variance jumps were recorded, and an FFT was calculated in Python (version 3.9.7) throughout a 1 s window: each window started at the detected strike time, using the `numpy.fft.fft()` function in the package NumPy (version 1.21.2). To extract the fundamental modes from the frequency data as calculated by the FFT, the `scipy.signal.find_peaks()` function in SciPy (version 1.7.1) was used to detect certain peaks that were within some particular width and above some peak prominence threshold. These parameters were tuned manually to ensure that only the apparent fundamental modes were detected and stored. The detected fundamental modes were averaged over all the strikes in each conducted test to generate a standard deviation associated with the detected fundamental modes.

5 EXPERIMENTAL RESULTS

5.1 Fiber Bragg Grating Test Results

Vibration data were obtained by striking the rod five times with a smaller metal rod to induce vibration at the larger rods natural frequencies. Vibration data were simultaneously recorded using the Hyperion/FBG setup and the LDV system. Although the fiber coupling method did not affect the LDV readings, it significantly affected the Hyperion/FBG readings. The first vibrational mode could be reliably detected in all four coupling combinations. However, resolving the second and third modes largely depended on how well the fiber was coupled to the rod. More robust coupling yielded clearer mode amplitudes, allowing the

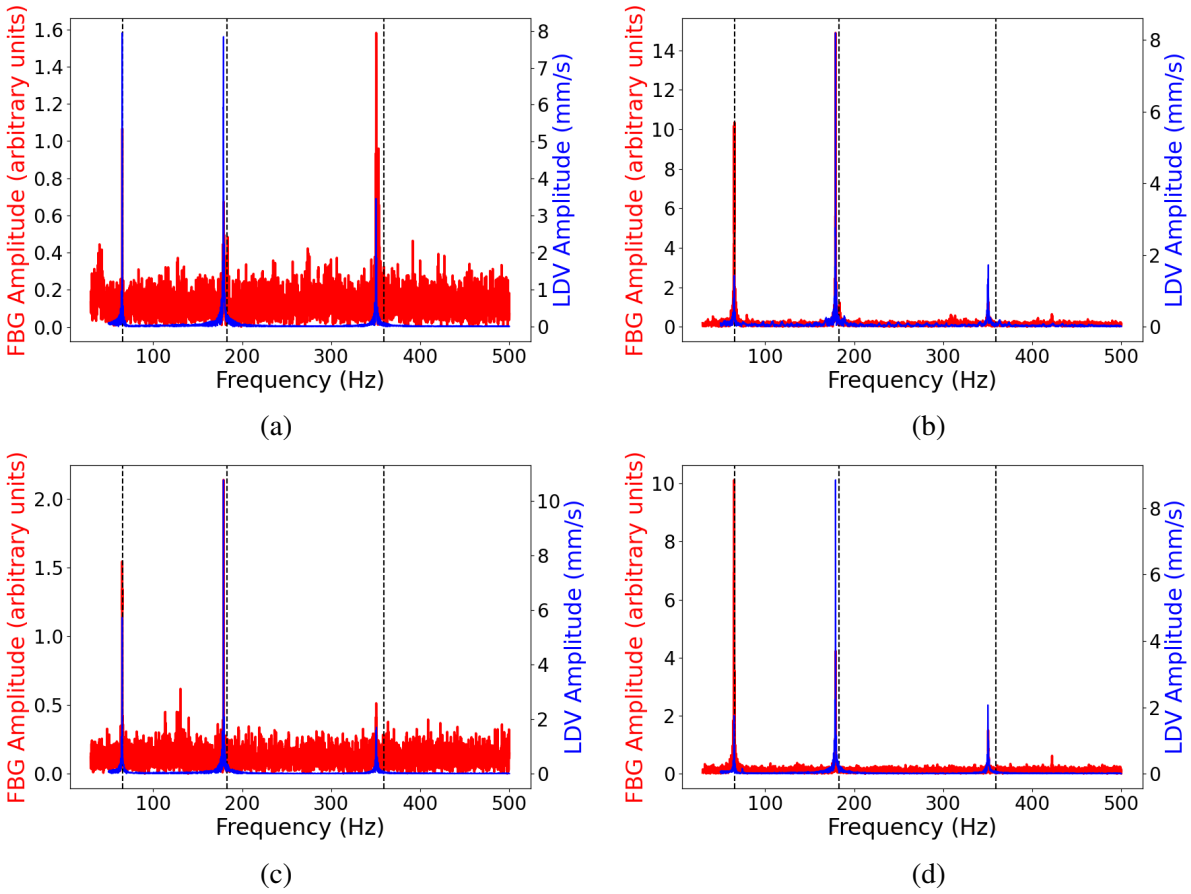

Figure 9. Measured vibrational spectra obtained using LDV and FBGs using four coupling methods: (a) bare fiber, taped at ends, (b) bare fiber, taped along the length, (c) fiber inserted into a tack-welded 0.25 mm inner diameter capillary, and (d) fiber inserted into a tack-welded and taped 0.25 mm inner diameter capillary.

vibrational wave to be plotted vs. position along the rod. Looser coupling methods resulted in unreliable detection of mode amplitudes and a high level of noise compared with the peak amplitude. Furthermore, the strength of the excitation strike may correlate with the ability to resolve the vibrational mode shape plots. At this time, it is unclear how much of the noise in the mode plots is due to the coupling mode or to the excitation method. One route of further exploration would be to repeat this experiment using a reproducible method of excitation with a known force.

For each coupling method, multiple tests were conducted, each measuring data from all 29 FBGs. Figure 9 shows the vibrational spectra acquired from one particular FBG (15 along the array) and the LDV for each coupling method. The dotted black lines represent the rod's theoretical resonant frequencies. The same FBG is considered in each plot to enable direct comparison at the same position; FBG 15 has a center wavelength of 1,540 nm. Overall, the noise levels and peak sharpness remained relatively consistent across all 29 FBGs within a dataset for a single coupling method. After obtaining peak frequencies and amplitudes for all FBGs using a peak-finding algorithm, the peak amplitudes for each of the three vibration modes—within the Hyperion bandwidth below the Nyquist criterion—were plotted along the length of the

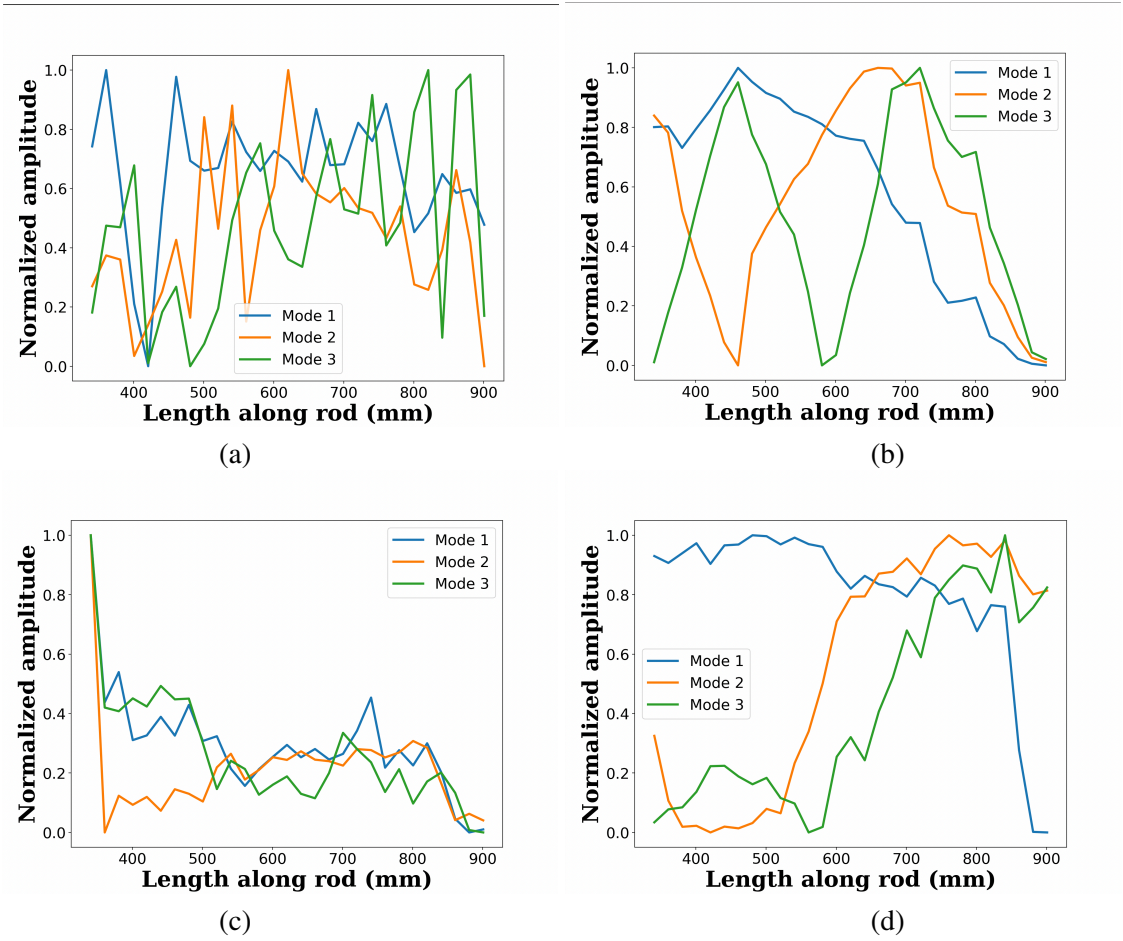

Figure 10. Normalized mode shapes measured using FBG fibers with four coupling methods: (a) bare fiber, taped at ends, (b) bare fiber, taped along the length, (c) fiber inserted into a tack-welded 0.25 mm inner diameter capillary, and (d) fiber inserted into a tack-welded and taped 0.25 mm inner diameter capillary.

rod, as shown in Figure 10. Only when the fiber was bonded along the entire length of the specimen (either within the capillary or as a bare fiber) do the mode shapes show resemblance to what is expected as per Euler-Bernoulli beam theory, in that the spatial oscillations occur with a smaller period as a function of increasing mode number [54].

All measured peak frequencies are listed in Table 1, along with the absolute value of the difference between the readings obtained from the FBGs vs. the LDV. The disagreement between the FBG and LDV readings was small: the largest discrepancy was only 0.22%.

5.2 High-Temperature Fabry–Pérot Cavity Frequency Response

The time-domain data corresponding with select tests within the temperature schedule defined in Figure 8 are shown in Figure 11. Specifically, the deflection data in the FPC and the voltage data from the accelerometer are shown for room-temperature tests before furnace firing, at a furnace set point of 400°C,

Table 1. Peak frequency measurements obtained from the FBGs and LDV for each coupling mode.

Specimen	LDV reading (Hz)	FBG reading (Hz)	Difference (%)
0.25 mm ID capillary, tack-weld + taped length			
Mode 1	65.3	65.3	0.05
Mode 2	179.1	179.3	0.11
Mode 3	350.2	350.4	0.07
0.25 mm ID capillary, tack-weld			
Mode 1	65.5	65.5	0.03
Mode 2	179.1	179.1	0.05
Mode 3	350.6	350.9	0.07
Bare fiber, taped along length			
Mode 1	65.6	65.7	0.08
Mode 2	179.1	179.1	0.05
Mode 3	350.6	350.5	0.03
Bare fiber, taped at ends			
Mode 1	65.3	65.5	0.22
Mode 2	179.1	179.3	0.11
Mode 3	350.3	350.5	0.06

and at a furnace set point of 800°C. Data are shown for tests both with and without the accelerometer bonded to the specimen. From the room-temperature tests in Figures 8.a and 8.b, the FPC deflects 10–15 nm from its average value upon striking the specimen strikes, and the average deflection does not vary significantly as a function of time during the room temperature tests. The FPC data in Figure 8.b show significantly longer resonance times than in Figure 8.a, demonstrating the extent to which the accelerometer damps the system compared with the configuration that only includes the FPC. The elevated temperature plots in Figures 8.c–8.f demonstrate how the average deflection drifts over the tens of seconds during which each test was conducted at higher temperatures. These drifts could be caused by thermal expansion/compaction effects imposed by thermal cycling of the furnace, or they could be related to time-dependent strain effects caused by oxidation or other phenomena. The specimen strikes induce deflections in the range of about 1–2 nm for the 400°C and 800°C tests, suggesting that the mechanical coupling between the nickel and copper could be weaker than it was during the room-temperature tests.

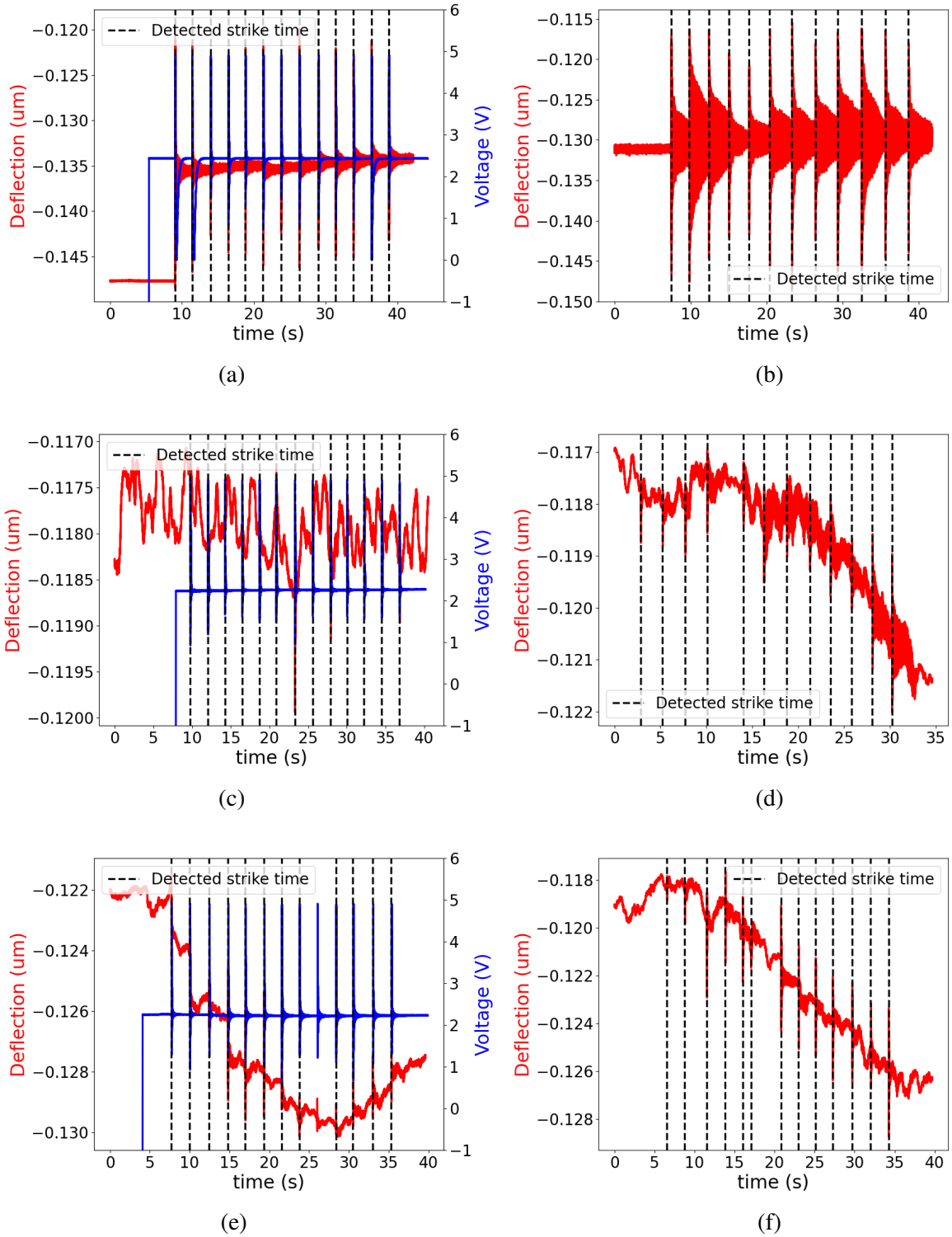

Figure 11. Measured FPC deflections with the LCI system and measured accelerometer voltage vs. time for different vibrational tests at different temperatures: room temperature with (a) accelerometer on and (b) FPC only; 400°C set point with (c) accelerometer on and (d) FPC only; 800°C set point with (e) accelerometer on and (f) FPC only.

The time-dependent deflection data following each strike shown in Figure 11 were processed using FFTs. The results are shown in Figure 12, which includes vibrational spectra at room temperature, at a furnace set point of 400°C, and at a furnace set point of 800°C. For all temperatures, the accelerometer's damping effect prevents clear resolution of the higher-order (>1) modes. This result is demonstrated either by the relatively large full width at half maximum of the peaks or by the absence of expected peaks when the accelerometer is attached. The theoretical modes were calculated using Euler–Bernoulli theory; the mathematical details are presented in a previous report [16]. These expected fundamental modes are shown in Figure 12 for room temperature only; the agreement between the experimental peaks and the theoretical fundamental modes is strongest for the room-temperature tests in Figures 12.a and 12.b. At the elevated temperatures, the experimental peak frequncies experience a discernible shift. This shift is expected, owing to the fundamental modes of the specimen. In general, particularly with the accelerometer removed, the FPC can resolve the first three fundamental modes for the test specimen, up to 800°C. Furthermore, the agreement between the FPC and the accelerometer for the fully resolved peaks is strong at all temperatures.

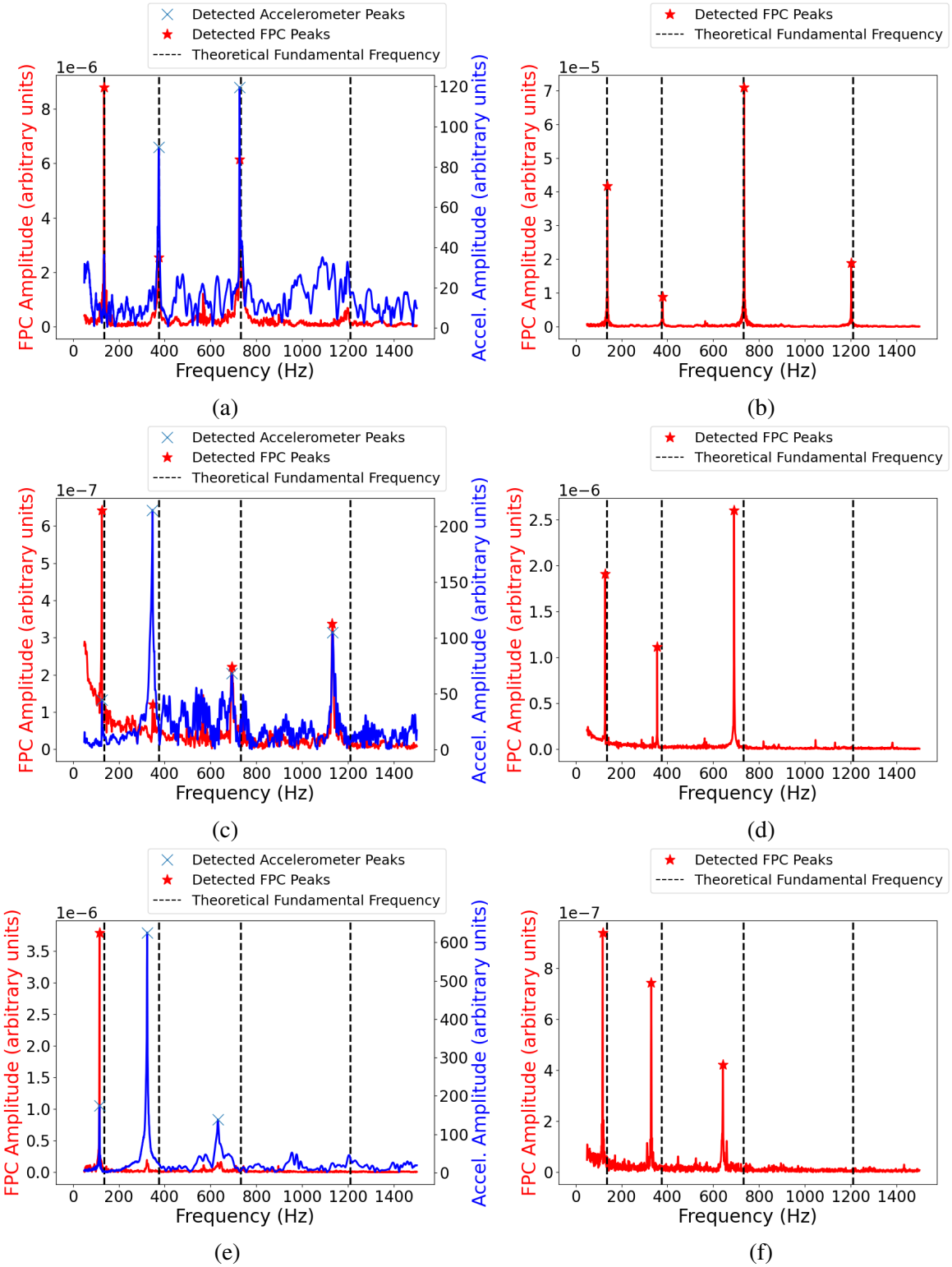

Figure 12. One-second FFTs of time domain data initiated on specimen strikes for the FPC and accelerometer voltage vs. time for different vibrational tests at different temperatures: room temperature with (a) accelerometer on and (b) FPC only; 400°C set point with (c) accelerometer on and (d) FPC only; 800°C set point with (e) accelerometer on and (f) FPC only.

To further assess the agreement between the FPC and the accelerometer, the detected fundamental (first) mode is plotted in Figure 13 as a function of temperature for results obtained using both sensors. The theoretical fundamental mode is shown with the assumption that the average specimen temperature is at either 100% or 75% of the set-point temperature. The theoretical frequency shift is based on changes in the coefficient of thermal expansion, density, and Young's modulus; these data have been reported by Shrivastava [55], Kim [56], and Kim [57], respectively. The error bars in Figure 13 are based on quadrature summation of the resolution of the FFT (1 Hz) and the standard deviation of the detected fundamental mode across all the strikes. Figure 13 confirms that, for the entire temperature schedule up to a furnace set point of 800°C, the accelerometer and the FPC agree within the margin of uncertainty. Furthermore, the extent to which the fundamental frequency shifts based on experimental measurements agrees reasonably well with theoretical shifts; the lack of knowledge of the specimen's true average temperature adds significant uncertainty to the comparison with theory and experimental data. Nevertheless, the results are clearly encouraging regarding the ability of the FPC to track expected shifts in resonant frequencies at high temperatures.

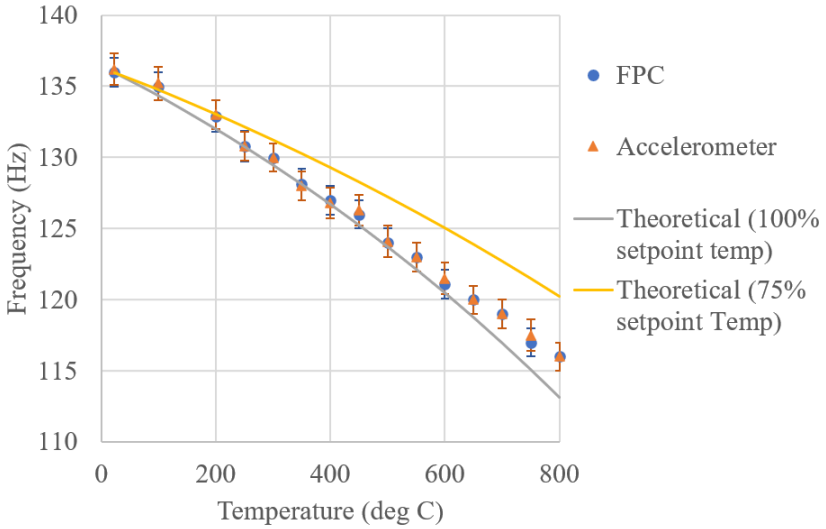

Figure 13. Changes in the resonant frequency of the fundamental mode as measured by the FPC and accelerometer as a function of temperature. The theoretical fundamental mode is also shown under the assumption that the specimen is at either 100% or 75% of the set-point temperature.

5.3 High-Temperature Fabry–Pérot Cavity Spectral Progression

Although the frequency content analyzed in the previous section yields a positive outlook on the FPC survivability at high temperatures, the reflected spectra from the FPCs is also useful in understanding potential sensor degradation modes at high temperatures. The reflected spectra as a function of temperature are plotted in Figure 14 during heating and cooling. The modulation in amplitude as a function of frequency is caused by the extent to which the light reflected by either fiber-end face constructively or destructively interferes. Based on the changes to the FSR, Figure 14.a indicates that the FPC expands during heating, and Figure 14.b suggests that the FPC shrinks during cooling. Unfortunately, the FPC completely lost signal at some point during cooling after 7.64 h. One interesting feature of Figure 14.a is the reduction in amplitude at about 200°C, followed by amplitude recovery at higher temperatures. This

feature could be a result of either a temporary misalignment of the fiber or a temporary obstruction in the light pathway in the cavity (e.g., epoxy residue), which was subsequently burned off. If the latter is the case, then certain preparations—such as ultrasonically bathing the capillary tube in ethanol or acetone or fabricating the FPC in a clean room—could prevent such issues.

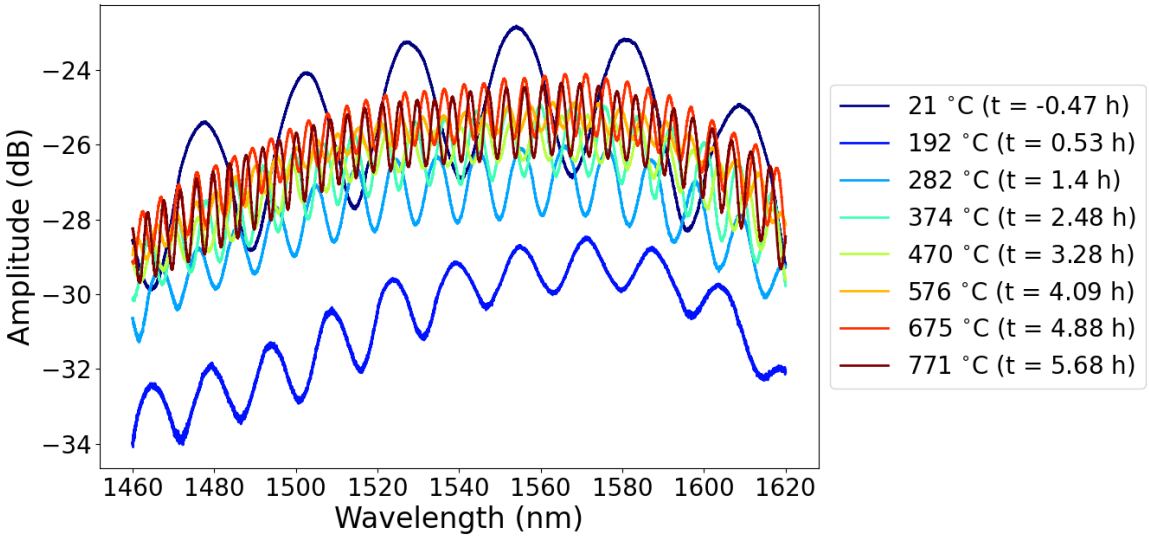

(a)

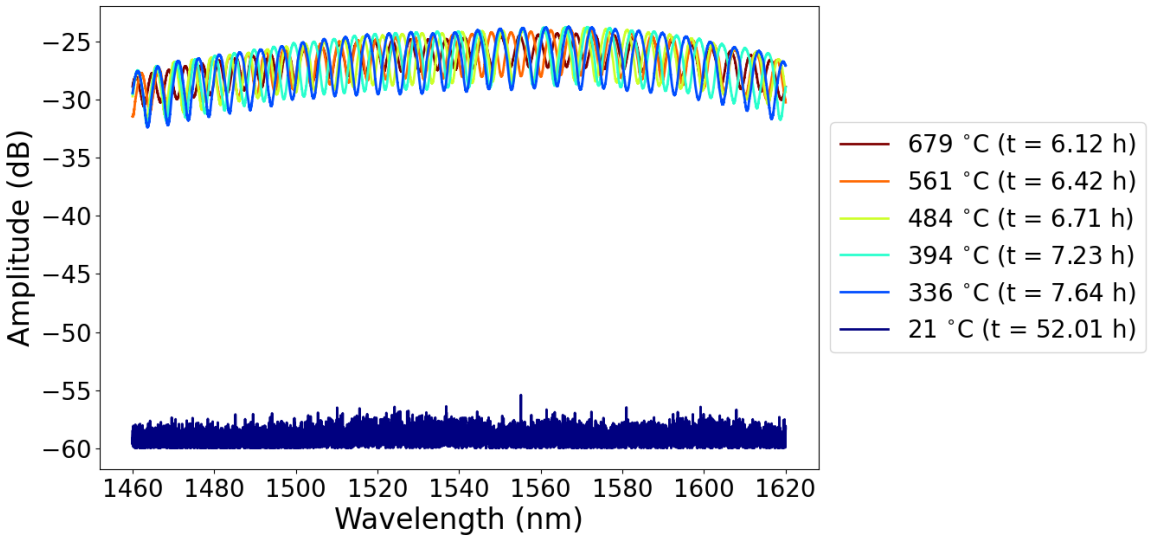

(b)

Figure 14. Reflected spectra from the FPC as measured by the Hyperion si155. (a) During the heating portion of the temperature profile and (b) during cooling.

Qualitatively, the expansion during heating and contraction during cooling was expected. Based on the

FSRs in Figure 14, the cavity length was calculated as a function of temperature as per the mathematics derived by Sweeney [47] and plotted in Figure 15. Note that the FSR is based on the mean peak to peak distance for all consecutive amplitude peaks in Figure 14, and the error bars are based on the standard deviation of the mean FSR. The slope of the cavity length vs. temperature curve is higher during heating compared to the slope during cooling, indicating that some hysteresis has occurred. Furthermore, there are apparent inflection points that are visible during heating. For example, the slope of the cavity length vs. temperature curve increases significantly beyond 100°C and then decreases between 400 and 500°C during heating, which may be the consequence of reduced coupling during heating. Overall, these observations could be explained by reduced mechanical coupling between the fiber and the capillary tube during cooling compared to the coupling during heating. This may have resulted from the fiber/capillary tube bond and/or the capillary tube/specimen bond yielding during heating.

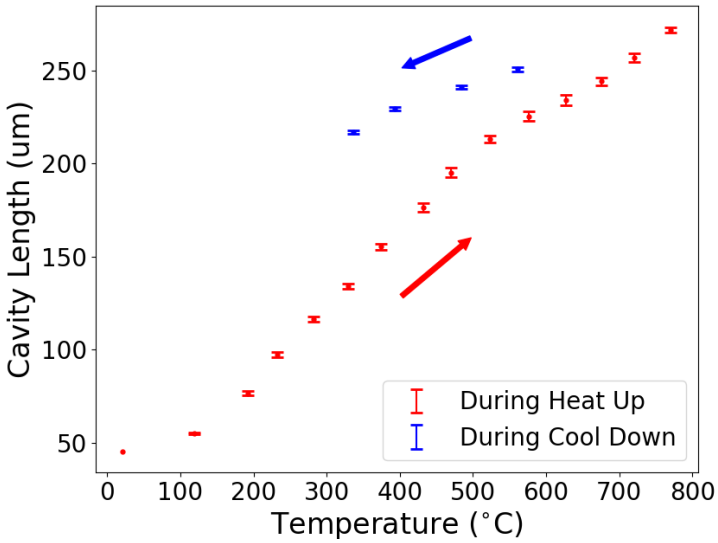

Figure 15. The cavity length of the FPC during heating and cooling as a function of temperature, determined based on the measured free spectral range.

There are two observations that may help explain the difference in behavior during heating vs. cooling. First, a temporary epoxy was applied to the fiber during fabrication of the FPC to bond it to the nickel capillary before laser bonding. This epoxy begins to break down at elevated temperatures, well below 800°C. This epoxy could have provided a temporary mechanical coupling between the fiber and the capillary tube until the epoxy thermally decomposed. Second, the nickel capillary and copper coating are exposed to oxygen in this test, and thus the formation of oxides in the interstitial space between the nickel and copper is expected. These oxides could affect the coupling between both materials and could have contributed to the general embrittlement of the sensor. This embrittlement could have prevented the fiber from surviving the full cooling cycle. Further investigation employing microscopy or x-ray imaging techniques is required to further investigate the trends illustrated in Figure 15.

6 CONCLUSION

The FBG and FPC optical fiber-based acoustic vibration sensors studied herein have both shown promise for applications in MRs. An FPC with a gap between two copper-coated fibers embedded in a nickel capillary, when interrogated with LCI, acts as a point sensor that enables accurate vibrational content measurements of the specimen to which the sensor is tack-welded, up to approximately 800°C. However, undesirable expansion characteristics and breakage upon cooling indicate that the FPC design needs further optimization. Finer tuning of the laser bonds that locally embed the fiber, investigation of other coating materials, and investigation of other capillary materials could yield a more robust sensor. The FPC design described herein represents a promising starting point in that regard. An array of type-I FBGs can enable accurate quasi-distributed vibrational measurements at room temperature, particularly when the bonding technique involves consistent mechanical coupling along the entire length of the specimen to which the FBG array is bonded. Perhaps the most promising result from the FBG tests is that, when the FBG array is inserted into a stainless-steel capillary tube and bonded along the entire length of a test specimen, the resultant mode shapes are clearly resolved, and the SNR of the vibrational content is relatively high. This result suggests that high-temperature FBG implementations up to expected MR operating temperatures, involving type-II FBGs in stainless-steel capillary tubes, would likely yield accurate quasi-distributed vibration measurements. Testing these type-II FBGs would be a logical next step for FBG development.

7 REFERENCES

[1] David E Shropshire, Geoffrey Black, and Kathleen Araujo. Global market analysis of microreactors. 7 2021.

[2] Shannon M Bragg-Sitton. Next generation nuclear energy: Advanced reactors and integrated energy systems. 4 2022.

[3] G Black, D Shropshire, K Araújo, and A van Heek. Prospects for nuclear microreactors: A review of the technology, economics, and regulatory considerations. *Nuclear Technology*, pages 1–20, 2022.

[4] Raffaella Testoni, Andrea Bersano, and Stefano Segantin. Review of nuclear microreactors: Status, potentialities and challenges. *Progress in Nuclear Energy*, 138:103822, 2021.

[5] Yasir Arafat and Jurie Van Wyk. evinci micro reactor. *Nucl. Plant J*, 37:34–36, 2019.

[6] Alison M Conner and George W Griffith. Evaluation of proposed oklo aurora microreactor sites at idaho national laboratory. Technical report, Idaho National Lab.(INL), Idaho Falls, ID (United States), 2020.

[7] Edward M. Duchnowski, Robert F. Kile, Kenny Bott, Lance L. Snead, Jason R. Trelewicz, and Nicholas R. Brown. Pre-conceptual high temperature gas-cooled microreactor design utilizing two-phase composite moderators. part i: Microreactor design and reactor performance. *Progress in Nuclear Energy*, 149:104257, 2022.

[8] J Wallenius, S Qvist, I Mickus, S Bortot, J Ejenstam, and P Szakalos. Sealer: a small lead-cooled reactor for power production in the canadian arctic. 2017.

[9] John H Jackson and Piyush Sabharwall. Foreword: Special issue on the us department of energy microreactor program, 2023.

[10] Christopher Matthews, Vincent Laboure, Mark DeHart, Joshua Hansel, David Andrs, Yaqi Wang, Javier Ortensi, and Richard C. Martineau. Coupled multiphysics simulations of heat pipe microreactors using direwolf. *Nuclear Technology*, 207(7):1142–1162, 2021.

[11] Jack Douglas Galloway, Valerie Jean Lawdensky, David Irvin Poston, Holly Renee Trellue, and Mikaela E. Blood. Effects of heat pipe failures in microreactors. 6 2020.

[12] Piyush Sabharwall, Jeremy Lee Hartvigsen, Terry James Morton, Zachary Don Sellers, and Jun Soo Yoo. Sphere assembly and operation demonstration. 12 2020.

[13] Holly Renee Trellue, James O'Brien, Robert Stowers Reid, Donna Guillen, and Piyush Sabharwall. Microreactor agile nonnuclear experimental testbed test plan. 1 2020.

[14] Yasir Arafat. Microreactor applications research, validation & evaluation (marvel) project. GAIN-NEI-EPRI Microreactor Workshop, Virtual, 2020.

[15] Idaho National Laboratory. A microreactor program plan for the department of energy, revision 3. Technical report, 2022. INL/EXT-20-58919.

[16] Anthony Birri, Dan Sweeney, Holden Hyer, and Christian Petrie. Status update on the development of transducers and bonding techniques for enabling acoustic measurements of damage in microreactor

components. Technical report, Oak Ridge National Lab.(ORNL), Oak Ridge, TN (United States), 2022.

[17] T. Fei, K. Mo, Y. Miao, C. Forsyth, R. Hu, S. Bhattacharya, and T. Kim. Conceptual core design of the molten metal fueled microreactor with self-regulating capability. *Annals of Nuclear Energy*, 173:109112, 2022.

[18] Scott William Doebling, Charles Reed Farrar, and Michael Bruce Prime. A summary review of vibration-based damage identification methods. *The Shock and Vibration Digest*, 30:91–105, 1998.

[19] Onur Avci, Osama Abdeljaber, Serkan Kiranyaz, Mohammed Hussein, Moncef Gabbouj, and Daniel J. Inman. A review of vibration-based damage detection in civil structures: From traditional methods to machine learning and deep learning applications. *Mechanical Systems and Signal Processing*, 147:107077, 2021.

[20] Vivek Agarwal, Kyle D. Neal, Sankaran Mahadevan, and Douglas Adams. Concrete structural health monitoring in nuclear power plants. 3 2017.

[21] Tadeusz Stepinski. Structural health monitoring of piping in nuclear power plants-a review of efficiency of existing methods. 2011.

[22] Shih-Yu Chu and Chan-Jung Kang. Development of the structural health record of containment building in nuclear power plant. *Nuclear Engineering and Technology*, 53(6):2038–2045, 2021.

[23] J. N. Eiras, C. Payan, S. Rakotonarivo, A. Spalvier, and V. Garnier. Vibration Monitoring of Nuclear Power Plant Containment Buildings During the Integrated Leakage Rate Test for Structural Condition Assessment. *Journal of Nondestructive Evaluation, Diagnostics and Prognostics of Engineering Systems*, 5(3), 02 2022. 031002.

[24] James William Sterbentz, James Elmer Werner, Michael George McKellar, Andrew John Hummel, John Charles Kennedy, Richard Neil Wright, and John Michael Biersdorf. Special purpose nuclear reactor (5 mw) for reliable power at remote sites assessment report. 4 2017.

[25] Kelly McCary, Brandon A. Wilson, Anthony Birri, Thomas E. Blue, and Christian M. Petrie. Suitability of type-ii fiber bragg gratings in silica optical fiber for temperature sensing in treat. 6 2019.

[26] Jinesh Mathew, Oliver Schneller, Dimitrios Polyzos, Dirk Havermann, Richard M. Carter, William N. MacPherson, Duncan P. Hand, and Robert R. J. Maier. In-fiber fabry–perot cavity sensor for high-temperature applications. *J. Lightwave Technol.*, 33(12):2419–2425, Jun 2015.

[27] Tianliang Li, Chaoyang Shi, Yuegang Tan, Ruiya Li, Zude Zhou, and Hongliang Ren. A diaphragm type fiber bragg grating vibration sensor based on transverse property of optical fiber with temperature compensation. *IEEE Sensors Journal*, 17(4):1021–1029, 2017.

[28] Atsushi Wada, Satoshi Tanaka, and Nobuaki Takahashi. Optical fiber vibration sensor using fbg fabryperot interferometer with wavelength scanning and fourier analysis. *IEEE Sensors Journal*, 12(1):225–229, 2012.

[29] Yoany Rodriguez Garcia, Jesus M Corres, and Javier Goicoechea. Vibration detection using optical fiber sensors. *Journal of Sensors*, 2010, 2010.

[30] Shengnan Wu, Liang Wang, Xiaolu Chen, and Bin Zhou. Flexible optical fiber fabryperot interferometer based acoustic and mechanical vibration sensor. *Journal of Lightwave Technology*, 36(11):2216–2221, 2018.

[31] Xin Liu, Baoquan Jin, Qing Bai, Yu Wang, Dong Wang, and Yuncai Wang. Distributed fiber-optic sensors for vibration detection. *Sensors*, 16(8):1164, 2016.

[32] Joshua T Jones, Daniel C Sweeney, Anthony Birri, Christian M Petrie, and Thomas E Blue. Calibration of distributed temperature sensors using commercially available smf-28 optical fiber from 22ř c to 1000ř c. *IEEE Sensors Journal*, 22(5):4144–4151, 2022.

[33] B Golubovic, BE Bouma, GJ Tearney, and JG Fujimoto. Optical frequency-domain reflectometry using rapid wavelength tuning of a cr 4+: forsterite laser. *Optics letters*, 22(22):1704–1706, 1997.

[34] Philippe Oberson, Benedikt Huttner, Olivier Guinnard, Laurent Guinnard, Grégoire Ribordy, and Nicolas Gisin. Optical frequency domain reflectometry with a narrow linewidth fiber laser. *IEEE Photonics Technology Letters*, 12(7):867–869, 2000.

[35] High-dose temperature-dependent neutron irradiation effects on the optical transmission and dimensional stability of amorphous fused silica. *Journal of Non-Crystalline Solids*, 525:119668, 2019.

[36] Christian M Petrie and Daniel C Sweeney. Enhanced backscatter and unsaturated blue wavelength shifts in f-doped fused silica optical fibers exposed to extreme neutron radiation damage. *Journal of Non-Crystalline Solids*, 615:122441, 2023.

[37] William Primak. Fast-neutron-induced changes in quartz and vitreous silica. *Physical Review*, 110(6):1240, 1958.

[38] Fan Piao, William G Oldham, and Eugene E Haller. The mechanism of radiation-induced compaction in vitreous silica. *Journal of non-crystalline solids*, 276(1-3):61–71, 2000.

[39] G Cheymol, L Remy, A Gusarov, Damien Kinet, Patrice Mégret, Guillaume Laffont, Thomas Blanchet, A Morana, E Marin, and S Girard. Study of fiber bragg grating samples exposed to high fast neutron fluences. *IEEE Transactions on Nuclear Science*, 65(9):2494–2501, 2018.

[40] Mohamed A.S. Zaghloul, Mohan Wang, Sheng Huang, Cyril Hnatovsky, Dan Grobnic, Stephen Mihailov, Ming-Jun Li, David Carpenter, Lin-Wen Hu, Joshua Daw, Guillaume Laffont, Simon Nehr, and Kevin P. Chen. Radiation resistant fiber bragg grating in random air-line fibers for sensing applications in nuclear reactor cores. *Opt. Express*, 26(9):11775–11786, Apr 2018.

[41] Yun Liu, Drew E. Winder, Bing Qi, Cary D. Long, and Wei Lu. Upgraded fiber-optic sensor system for dynamic strain measurement in spallation neutron source. *IEEE Sensors Journal*, 21(23):26772–26784, 2021.

[42] Zhen Chen, Lei Yuan, Gerald Hefferman, and Tao Wei. Ultraweak intrinsic fabry–perot cavity array for distributed sensing. *Optics letters*, 40(3):320–323, 2015.

[43] Ping Xu, Fufei Pang, Na Chen, Zhenyi Chen, and Tingyun Wang. Fabry-perot temperature sensor for quasi-distributed measurement utilizing otdr. In *2008 1st Asia-Pacific Optical Fiber Sensors Conference*, pages 1–4. IEEE, 2008.

[44] Edvard Cibula and Denis Donlagic. In-line short cavity fabry-perot strain sensor for quasi distributed measurement utilizing standard otdr. *Optics Express*, 15(14):8719–8730, 2007.

[45] Bin Du, Jun He, Baijie Xu, Xizhen Xu, Cailing Fu, Pengfei Li, Xunzhou Xiao, Shen Liu, Yatao Yang, and Yiping Wang. High-density weak in-fiber micro-cavity array for distributed high-temperature sensing with millimeter spatial resolution. *Journal of Lightwave Technology*, 40(22):7447–7455, 2022.

[46] Ying Huang, Tao Wei, Zhi Zhou, Yinan Zhang, Genda Chen, and Hai Xiao. An extrinsic fabry–perot interferometer-based large strain sensor with high resolution. *Measurement Science and Technology*, 21(10):105308, 2010.

[47] Daniel C. Sweeney, Anthony Birri, and Christian M. Petrie. Hybrid method for monitoring large Fabry-Pérot cavity displacements with nanometer precision. *Optics Express*, 30(16):29148–29160, Aug 2022.

[48] Bing Qi, Drew E Winder, and Yun Liu. Quadrature phase-shifted optical demodulator for low-coherence fiber-optic fabry-perot interferometric sensors. *Optics Express*, 27(5):7319–7329, 2019.

[49] Daniel C Sweeney, Adrian M Schrell, Yun Liu, and Christian M Petrie. Metal-embedded fiber optic sensor packaging and signal demodulation scheme towards high-frequency dynamic measurements in harsh environments. *Sensors and Actuators A: Physical*, 312:112075, 2020.

[50] Daniel C Sweeney, Adrian M Schrell, and Christian M Petrie. Compensation scheme for radiation-induced attenuation in optical fibers interrogated using low-coherence interferometry. volume 122, pages 291–294. American Nuclear Society, 2020.

[51] A.N. Sinclair and A.M. Chertov. Radiation endurance of piezoelectric ultrasonic transducers a review. *Ultrasonics*, 57:1–10, 2015.

[52] P. Castellini, M. Martarelli, and E.P. Tomasini. Laser doppler vibrometry: Development of advanced solutions answering to technology's needs. *Mechanical Systems and Signal Processing*, 20(6):1265–1285, 2006.

[53] et al Petrie, Christian M. Embedded metallized optical fibers for high temperature applications. *Smart Materials and Structures*, 28(5):055012–055012, 2019. Special Issue: Laser Doppler Vibrometry.

[54] João Silva, Lucas Nascimento, and Simone dos Santos. Free vibration analysis of euler-bernoulli beams under non-classical boundary conditions. In *IX Congresso Nacional de Engenharia Mecânica*, Fortaleza, Brazil, 2015.

[55] Aroh Shrivastava, Vrushabh Lambade, and Paritosh Chaudhuri. Measurement of thermal expansion for stainless steel 304, copper, aluminium and brass by push rod dilatometry. Technical report, Institute for Plasma Research, Bhat, Near Indira Bridge, Gandhinagar, 2020. IPR/TR-603/2020.

[56] Choong S Kim. Thermophysical properties of stainless steels. Technical report, Argonne National Lab., Ill.(USA), 1975.

[57] Bong Goo Kim, Joy Rempe, Darrell Knudson, Keith Condie, and Bulent Sencer. In-situ creep testing capability for the advanced test reactor. *Nuclear technology*, 179:413–428, 09 2012.